

# The high-energy frontier of the muon $g-2$

PARIDE PARADISI<sup>a,b</sup>, OLCYR SUMENSARI<sup>c</sup>, ALESSANDRO VALENTI<sup>b,a</sup>

<sup>a</sup> *Istituto Nazionale Fisica Nucleare, Sezione di Padova, I-35131 Padova, Italy*

<sup>b</sup> *Dipartimento di Fisica e Astronomia “G. Galilei”, Università di Padova, Italy*

<sup>c</sup> *IJCLab, Pôle Théorie (Bât. 210), CNRS/IN2P3 et Université Paris-Saclay, 91405 Orsay, France*

## Abstract

The long-standing muon  $g-2$  anomaly can be explained by heavy new physics particles through chirally-enhanced contributions. It has been recently proposed that a muon collider running at center-of-mass energies of several TeV could test these new physics scenarios in a model-independent way, through the study of high-energy processes such as  $\mu^+\mu^- \rightarrow h\gamma$ . In this work, we validate these findings, based on effective field theories, by considering renormalizable simplified models and by computing this one-loop process in full generality. Furthermore, we explore the interplay of direct and indirect high-energy searches to pin down the details of the underlying new physics model accommodating the muon  $g-2$  anomaly.

# 1 Introduction

The anomalous magnetic moment of the muon  $a_\mu = (g_\mu - 2)/2$  represents one of the most interesting and long-standing hints for New Physics (NP). Recently, the E989 experiment at Fermilab [1] has confirmed previous results by the E821 experiment at BNL [2], yielding the experimental average  $a_\mu^{\text{EXP}} = 116592061(41) \times 10^{-11}$ . Comparing this value with the Standard Model (SM) prediction  $a_\mu^{\text{SM}} = 116591810(43) \times 10^{-11}$ , reported by the Muon  $g-2$  Theory Initiative [3], leads to an interesting  $4.2\sigma$  discrepancy [1]<sup>1</sup>

$$\Delta a_\mu = a_\mu^{\text{EXP}} - a_\mu^{\text{SM}} = 251(59) \times 10^{-11}. \quad (1.1)$$

Since the observed deviation is comparable in size to the SM electroweak contribution, it would be natural to invoke new weakly-coupled particles at the electroweak scale to solve this puzzle. However, this possibility is strongly disfavoured by LEP and LHC data which push the NP scale  $\Lambda$  to lie above  $\Lambda \gtrsim 1$  TeV.<sup>2</sup>

Heavy NP contributions to  $\Delta a_\mu$  are captured by the dimension-6 operator  $(\bar{\mu}_L \sigma_{\mu\nu} \mu_R) H F^{\mu\nu}$  [8], where  $H$  is the SM Higgs doublet and  $F^{\mu\nu}$  denotes the electromagnetic field strength tensor. After electroweak symmetry breaking,  $\Delta a_\mu$  receives the contribution  $\Delta a_\mu \sim (g_{\text{NP}}^2/16\pi^2) \times (m_\mu v/\Lambda^2)$ , where  $v = 246$  GeV is the electroweak vacuum-expectation-value (vev) and  $g_{\text{NP}}$  denotes a generic NP coupling. Therefore, the NP chiral enhancement  $v/m_\mu \sim 10^3$  brings the sensitivity of  $\Delta a_\mu$  to NP scales of order  $\Lambda \sim 10$  TeV even for weak couplings  $g_{\text{NP}} \sim 1$  [9, 10]. The same dipole operator generating  $\Delta a_\mu$  induces also a NP contribution to the process  $\mu^+\mu^- \rightarrow h\gamma$  that grows quadratically with the center-of-mass energy  $\sqrt{s}$  of the collisions, as recently demonstrated in the context of Effective Field Theories (EFT) [11]. Therefore, measuring the cross-section of  $\mu^+\mu^- \rightarrow h\gamma$  would be equivalent to measuring  $\Delta a_\mu$ . This goal can be achieved at a multi-TeV muon collider [12].

In this work, we revisit the connection between  $\Delta a_\mu$  and  $\mu^+\mu^- \rightarrow h\gamma$  within simplified models which induce chirally-enhanced contributions to  $\Delta a_\mu$ . In particular, we focus on models with new scalars and vector-like fermions in various  $SU(2)_L \times U(1)_Y$  representations, with an underlying  $Z_2$  symmetry to prevent dangerous mixing of the new states with SM fields [13]. As already discussed in Ref. [13], where the matching of these models onto the relevant set of dimension-6 SMEFT operators [8] has been performed, these scenarios display correlations between  $\Delta a_\mu$  and other processes such as  $h \rightarrow \mu^+\mu^-$  and  $Z \rightarrow \mu^+\mu^-$ . Moreover, such models generally contain a stable particle and therefore they can also explain the observed dark matter relic abundance [14, 15].

The first goal of our analysis is to validate the findings of previous EFT studies [11] by performing a full one-loop calculation of the  $\mu^+\mu^- \rightarrow h\gamma$  cross-section within the simplified models of Ref. [13]. As our results hold for any center-of-mass energy value  $\sqrt{s}$ , they will complement the findings of Ref. [11], which only apply in the EFT regime  $\sqrt{s} \ll \Lambda$ , and they will allow us to precisely assess the validity limit of the EFT description for this particular process. Another goal of our work is to study the direct searches signatures of these simplified models (see also Ref. [10]). On general grounds, the discovery of new particles by their direct production can be hardly associated in a non-ambiguous way to  $\Delta a_\mu$ . However, this statement strictly applies only to  $2 \rightarrow 2$  processes as they are not sensitive to the same combination of parameters entering  $\Delta a_\mu$ . Instead, we point out that  $2 \rightarrow 3$  processes with a Higgs boson in the final state are in one-to-one correspondence with  $\Delta a_\mu$  and also

<sup>1</sup>Recently, a lattice QCD collaboration computed the leading hadronic contribution to the muon  $g-2$  with a comparable precision to the dispersive determinations, finding a larger value which weakens the discrepancy to  $1.6\sigma$  [4]. However, this increase to the hadronic contribution could imply tensions with the electroweak fit, or with low-energy  $e^+e^- \rightarrow \text{hadron}$  data [5]. For this reason, the findings of Ref. [4] should be verified by independent lattice QCD studies which are underway or by direct experimental measurements, as proposed by the MUonE experiment [6].

<sup>2</sup>Other viable solutions are provided by very light and feebly coupled NP particles such as axion-like particles [7].

with  $\mu^+\mu^- \rightarrow h\gamma$ . The correlated study of these observables at a muon collider allows to disentangle among the underlying NP model accommodating the  $\Delta a_\mu$  anomaly, therefore representing a very interesting example of the interplay of the high-energy and high-intensity frontiers of particle physics.

The paper is organised as follows. In section II, we introduce the simplified models and their predictions for the muon  $g-2$ . In section III, we focus on indirect high-energy probes of the muon  $g-2$  at a muon collider, by computing the one-loop induced process  $\mu^+\mu^- \rightarrow h\gamma$  in the context of simplified models and by establishing the limit of validity of the EFT results. In section IV, we analyse direct high-energy probes of the muon  $g-2$  at a muon collider which include both  $2 \rightarrow 2$  and  $2 \rightarrow 3$  scattering processes. Our final remarks and conclusions are made in Sec. V.

## 2 Simplified models for the muon $g-2$

We consider the two classes of simplified models that can provide a chiral enhancement to  $\Delta a_\mu$ , which consist in extending the SM with two scalars  $\Phi_{L,E}$  and one vector-like fermion  $\Psi$  (model I), or two vector-like fermions  $\Psi_{L,E}$  and one scalar  $\Phi$  (model II). These models are generically described by the following Lagrangians [13, 15],

$$\mathcal{L}_I = \lambda_L^I \bar{\ell} \Psi \Phi_L + \lambda_E^I \bar{e} \Psi \Phi_E + A \Phi_L^\dagger \Phi_E H + \text{h.c.}, \quad (2.1)$$

$$\mathcal{L}_{II} = \lambda_L^{II} \bar{\ell} \Psi_L \Phi + \lambda_E^{II} \bar{e} \Psi_E \Phi + \kappa \bar{\Psi}_L \Psi_E H + \text{h.c.}, \quad (2.2)$$

where  $\ell$  and  $e$  are the SM lepton doublet and singlet, respectively, and  $H$  denotes the SM Higgs doublet. Note, in particular, that we have imposed an underlying  $Z_2$  symmetry to prevent dangerous mixing of the new states with SM fields [13]. By restricting the  $SU(2)_L$  representations of  $\Psi_{(L,E)}$  and  $\Phi_{(L,E)}$  up to triplets, there are four possibilities in each of these models. The allowed  $SU(2)_L \times U(1)_Y$  representations are listed in Table 1, where  $X$  denotes the hypercharge of the field  $\Psi$  ( $\Phi$ ) for the models of type I (type II). The respective Lagrangians are spelled out in Appendix A where the  $SU(2)_L$  contractions are explicitly written.<sup>3</sup>

	$R$	$\Psi, \Phi$	$\Phi_L, \Psi_L$	$\Phi_E, \Psi_E$
$SU(2)_L$	121	1	2	1
	212	2	1	2
	323	3	2	3
	232	2	3	2
$Y$		$X$	$-\frac{1}{2} - X$	$-1 - X$

Table 1: Charge assignments and representations under  $SU(2)_L \times U(1)_Y$  for the NP states.

The simplified models listed in Table 1 contribute to  $\Delta a_\mu$  via the loop diagrams depicted in Fig. 1. These new interactions are assumed to arise at the energy scale  $\Lambda$ , which lies well above the electroweak scale, in such a way that their contributions to  $\Delta a_\mu$  can be fully interpreted in terms of the SMEFT Lagrangian [8],

$$\mathcal{L}_{\text{SMEFT}} \supset C_{eB} (\bar{\ell} \sigma^{\mu\nu} e) H B_{\mu\nu} + C_{eW} (\bar{\ell} \sigma^{\mu\nu} e) \tau^I H W_{\mu\nu}^I + \text{h.c.} \quad (2.3)$$

<sup>3</sup>The new particles could also be charged under  $SU(3)_c$ , which would amount to multiplicative representation-dependent factors in the expressions derived in this paper. In particular the fermions  $\Psi_{L,E}$  in model II could be the top-quark, recovering the minimal leptoquark solution to  $\Delta a_\mu$  where  $\Phi$  could be either the state  $(3, 2, 7/6)$  or  $(\bar{3}, 1, 1/3)$  [16]. Instead, scenarios with two scalar leptoquarks are fully described by model I upon matching Ref. [17].

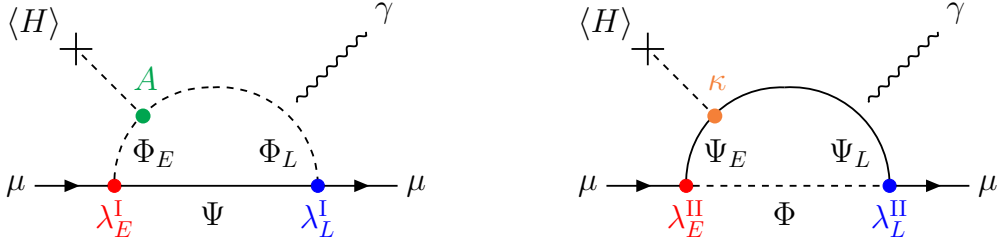


Figure 1: Feynman diagrams contributing to the muon  $g-2$  at one-loop level in the simplified models I (left panel) and II (right panel).

where we have only written the  $d = 6$  operators that are relevant in our setup, and where flavor indices are omitted. The leading contributions to  $\Delta a_\ell$  can then be written as

$$\Delta a_\ell \simeq \frac{4m_\ell v}{\sqrt{2}e} \text{Re}(C_{e\gamma}) , \quad (2.4)$$

where the effective coefficient  $C_{e\gamma}^\ell = \cos\theta_W C_{eB}^\ell - \sin\theta_W C_{eW}^\ell$  can be expressed, for the simplified models I and II, in a very compact form

$$[C_{e\gamma}]_I = -\frac{e\text{Re}[\lambda_L^I(\lambda_E^I)^* A]}{384\pi^2 M^3} \{2X + 1, -2X, 6X - 1, 2(3X + 2)\} , \quad (2.5)$$

$$[C_{e\gamma}]_{II} = \frac{e\text{Re}[\lambda_L^{II}(\lambda_E^{II})^* \kappa]}{384\pi^2 M^2} \{2(X + 1), -(2X + 1), 2(3X + 1), 6X + 7\} , \quad (2.6)$$

where a degenerate mass  $M$  is assumed for the NP states. The expressions between brackets give the hypercharge factors for the  $SU(2)_L$  representations  $R = \{121, 212, 323, 232\}$  of Table 1. Our results shown in Eqs. (2.5) and (2.6) are in full agreement with those from Ref. [13].

Since we are interested in scenarios with new particles in the multi-TeV range, an explanation of the muon  $g-2$  anomaly would necessarily require  $\mathcal{O}(1)$  Yukawa couplings. In particular, one typically finds that a contribution of order  $\Delta a_\mu \sim 10^{-9}$  can be obtained for  $\lambda_L, \lambda_E, \kappa \sim 2$ ,  $A/M \sim 1$  and  $M \sim 10$  TeV. For such large couplings, a natural question concerns the quantum stability of these simplified models.

The one-loop running of the model parameters for the various choices of the  $SU(2)_L \times U(1)_Y$  representations is reported in detail in Appendix A. As a result of this analysis, we show in Fig. 2 (left and center panels) the Landau poles of the new coupling constants  $\lambda_L$ ,  $\lambda_E$  and  $\kappa$  for the representation  $R = 121$  setting  $M = 10$  TeV and  $X = 1/2$ . By requiring that these couplings do not develop a Landau pole below  $10^3$  TeV, we conclude that they should be smaller than  $\approx 3$ . In the right panel, we also plot the location of the Landau pole of the SM gauge coupling  $g'$  as a function of the hypercharge  $X$ . Clearly, the absolute value of  $X$  cannot be arbitrarily large, otherwise  $g'$  would develop a pole well below the Planck scale. By combining these indirect bounds, we infer that the simplified scenarios can only be self-consistent, while explaining explain the  $\Delta a_\mu$  discrepancy, if the mass  $M$  is below  $\lesssim 15$  TeV. These conclusions have been obtained for the representation  $R = 121$  and  $X = 1/2$ , but they can be easily generalized to the other scenarios. Note, in particular, that in the presence of weak triplets, one should also worry about the Landau poles of the  $SU(2)_L$  gauge coupling  $g$  since its  $\beta$ -function becomes positive for some of the models from Table 1.

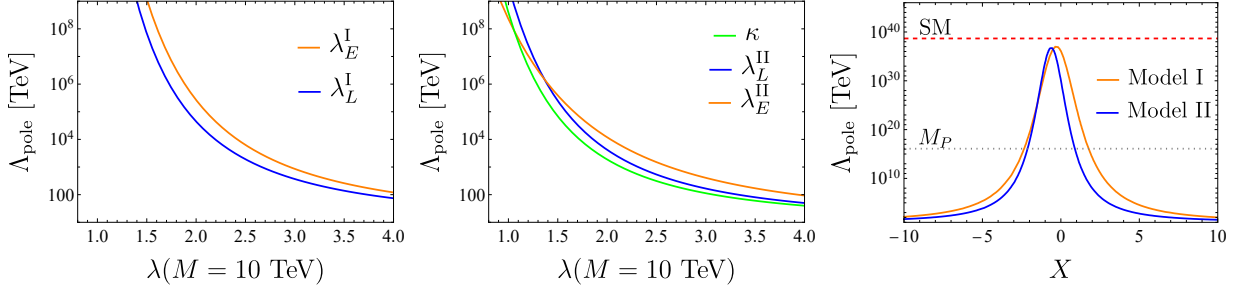


Figure 2: Landau poles of the new coupling constants of the simplified models I (left) and II (center) for the representation  $R = 121$  (see Appendix A) setting  $M = 10$  TeV and  $X = 1/2$ . The plot on the right shows the location of the Landau pole of the SM gauge coupling  $g'$  as a function of  $X$ .

### 3 Indirect high-energy probes of the muon $g - 2$

As recently discussed in Ref. [11], an interesting signature which inevitably accompanies NP contributions to  $\Delta a_\mu$  is the modification to the process  $\mu^+\mu^- \rightarrow h\gamma$  at high-energies, which could be a target of the proposed muon collider [12]. This complementarity becomes clear when comparing the Feynman diagrams depicted in Figs. 1 and 3. In this section, we will compute the cross-section of  $\mu^+\mu^- \rightarrow h\gamma$  in the simplified models outlined above. Since our results will be valid for any center-of-mass energy value  $\sqrt{s}$ , they will complement the results of Ref. [11] which only apply in the EFT regime  $\sqrt{s} \ll \Lambda$ . As a by-product, the comparison between the computations made within concrete scenarios and the corresponding EFTs will allow us to precisely assess the limits of the EFT description for this particular process.

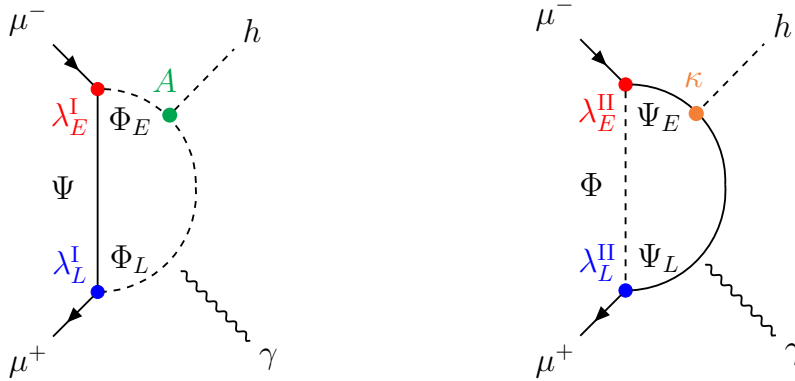


Figure 3: Feynman diagrams contributing to the high-energy scattering  $\bar{\mu}\mu \rightarrow h\gamma$  for the simplified models I (left panel) and II (right panel).

We start by writing the most general Lorentz-invariant amplitude contributing to  $\mu^+\mu^- \rightarrow h\gamma$ ,

$$\begin{aligned} \mathcal{A}_\mu = \bar{v}(p_2) [ & A\gamma_\mu + B(p_1 + p_2)_\mu + Ck_\mu + D\sigma_{\mu\nu}k^\nu + E\sigma_{\mu\nu}(p_1 + p_2)^\nu \\ & + A'\gamma_\mu\gamma_5 + B'\gamma^5(p_1 + p_2)_\mu + C'\gamma^5k_\mu + D'\gamma^5\sigma_{\mu\nu}k^\nu + E'\gamma^5\sigma_{\mu\nu}(p_1 + p_2)^\nu ] u(p_1), \end{aligned} \quad (3.1)$$

where  $p_1$ ,  $p_2$  and  $k$  denotes the momentum of  $\mu^-$ ,  $\mu^+$  and  $\gamma$ , respectively. In this expression we exploited momentum conservation,  $q^\mu = p_1^\mu + p_2^\mu - k^\mu$ , and neglected the masses of the external

states. The form factors  $\{A^{(\prime)}, B^{(\prime)}, \dots\}$  are functions of the Mandelstam variables  $s, t$  and  $u$  defined as follows,

$$s = (p_1 + p_2)^2, \quad t = (p_1 - k)^2, \quad u = (p_2 - k)^2, \quad (3.2)$$

which satisfy  $s + t + u \approx 0$ . The expression of Eq. (3.1) has been obtained taking into account that:

- The Gordon's identity and the Dirac equation allow to trade  $\sigma^{\mu\nu}(p_1 \mp p_2)_\nu$  for  $(p_1 \pm p_2)^\mu$  in the massless muon limit. The same holds for the corresponding terms with an extra  $\gamma^5$ ;
- A possible term  $\bar{v} \epsilon_{\mu\nu\rho\sigma} p_1^\nu p_2^\rho k^\sigma u$  containing the Levi-Civita tensor  $\epsilon_{\mu\nu\rho\sigma}$  is not independent. In fact, we can write  $\epsilon_{\mu\nu\rho\sigma} = -i\gamma^5 \gamma_{[\mu} \gamma_\nu \gamma_\rho \gamma_{\sigma]}$ , reducing this term to  $\bar{v} \gamma^\mu p_1^\nu p_2^\rho k^\sigma u + \text{permutations}$ . Then, by using  $\not{a}\not{b} = a \cdot b - i\sigma^{\mu\nu} a_\mu b_\nu$ , we are able to recast this term as a linear combination of the ones already listed in Eq. (3.1). The same is true for the term  $\bar{v} \gamma_5 \epsilon_{\mu\nu\rho\sigma} p_1^\nu p_2^\rho k^\sigma u$ .

Furthermore, Eq. (3.1) can be simplified by imposing that the amplitude  $\mathcal{A}_\mu$  is gauge invariant, that is imposing the QED Ward identity  $k^\mu \mathcal{A}_\mu = 0$ . As a result, we find that  $A = A' = 0$ ,  $B' = -iE'$  and  $sB = (u - t)iE$ . Finally, dropping the irrelevant  $k_\mu$  term which gives a vanishing contribution for on-shell photons, we can write the amplitude in a very compact form

$$\begin{aligned} \mathcal{A}^\mu = \bar{v}(p_2) & \left[ \mathcal{D} i\sigma^{\mu\nu} k_\nu + \mathcal{F} \left( \frac{t-u}{s} (p_1 + p_2)^\mu - \frac{t+u}{s} (p_1 - p_2)^\mu \right) \right. \\ & \left. + \mathcal{D}' i\sigma^{\mu\nu} \gamma_5 k_\nu + \mathcal{F}' \left( \frac{t-u}{s} (p_1 + p_2)^\mu - \frac{t+u}{s} (p_1 - p_2)^\mu \right) \gamma_5 \right] u(p_1), \end{aligned} \quad (3.3)$$

where  $\mathcal{D}^{(\prime)}$  and  $\mathcal{F}^{(\prime)}$  are the only independent form-factors, which are defined as linear combinations of the ones defined above. The  $\mu^+ \mu^- \rightarrow h\gamma$  differential cross-section can then be written as

$$\frac{d\sigma_{h\gamma}}{dt} = \frac{tu}{16\pi s^2} \left( |\mathcal{D} + \mathcal{F}|^2 + |\mathcal{F}|^2 + |\mathcal{D}' + \mathcal{F}'|^2 + |\mathcal{F}'|^2 \right). \quad (3.4)$$

We are now ready to calculate the analytical expressions of the form factors  $\mathcal{D}^{(\prime)}$  and  $\mathcal{F}^{(\prime)}$  in the simplified models I and II.

Our approach is to evaluate the amplitudes associated with the Feynman diagrams of Fig. 3 and then to project them into the form factors of Eq. (3.3). The results of our full computation will be presented in Sec. 3.1. The discussion for the EFT limit for the form-factors will be made in Sec. 3.2 and our numerical results will be presented in Sec. 3.3.

### 3.1 $\mu^+ \mu^- \rightarrow h\gamma$ in simplified models

In this section, we explicitly evaluate the form-factors  $\mathcal{D}^{(\prime)}$  and  $\mathcal{F}^{(\prime)}$  at one-loop for the simplified models defined in Eq. (2.2). Our convention for the kinematical variables is given in Eq. (3.2) and we use `Package-X` [19] to reduce the one-loop integrals in terms of the Passarino-Veltman functions. The masses of the external states are neglected and, for simplicity, we assume a degenerate mass  $M$  for the new scalar and vector-like fermion running in the loops. In order to obtain general results for all the models appearing in Table 1, we define the coefficients  $\xi$  and  $\tilde{\xi}$  in Table 2 which depend on the  $SU(2)_L$  representation  $R$  that is considered.<sup>4</sup>

<sup>4</sup>These coefficients can be compared to Ref. [13] by identifying  $\xi \leftrightarrow \xi_{eB}$ ,  $\tilde{\xi} \leftrightarrow \tilde{\xi}_{eW}$  and noting that their extra two coefficients are not independent, i.e.  $\xi_{eW}^E = -\xi_{eW}$ ,  $\xi_{eW}^L = -\xi_{eW} + \xi_{eB}/2$ . The last relations follow from gauge invariance and can be obtained, for instance, by explicitly checking the Ward identity in the  $\mu^+ \mu^- \rightarrow h\gamma$  amplitude.

$R$	121	212	323	232
$\xi$	1	-1	3	3
$\tilde{\xi}$	0	$-\frac{1}{2}$	2	$-\frac{1}{2}$

Table 2: Representation-dependent factors  $\xi$  entering the  $\mu^+\mu^- \rightarrow h\gamma$  calculation for each of the models defined in Table 1.

The ultraviolet divergences, arising from the reducible diagrams with the photon attached to the external muons, are eliminated, as usual, by the counter-term for the muon Yukawa coupling due to the new interactions. In particular for the models of type-I there are no such divergences, since all the diagrams are UV-finite. In this case we still add a counterterm to obtain an amplitude depending only on the physical Yukawa coupling.

**Model I:** For the simplified model I, we find the following results,

$$\mathcal{D} = \frac{ieM\text{Re}[\lambda_L^I(\lambda_E^I)^*A]}{32\sqrt{2}\pi^2tu} \left[ 2(\xi X - \tilde{\xi})tuD_0(0, 0, 0, 0, u, t; \mathbf{M}) - 2\xi uC_0(0, 0, t; \mathbf{M}) - \xi tC_0(0, 0, u; \mathbf{M}) + \xi \frac{s}{M^2} \right], \quad (3.5)$$

$$\begin{aligned} \mathcal{F} = & -\frac{ieM\text{Re}[\lambda_L^I(\lambda_E^I)^*A]}{32\sqrt{2}\pi^2tu} \left[ (\xi(1+X) - \tilde{\xi}) suD_0(0, s, 0, u, 0, 0; \mathbf{M}) + tu(\xi X - \tilde{\xi})D_0(0, 0, 0, 0, u, t; \mathbf{M}) \right. \\ & + st(\xi(1+X) - \tilde{\xi})D_0(0, s, 0, t, 0, 0; \mathbf{M}) + 2(\xi s + (\tilde{\xi} - \xi X)u)C_0(0, 0, u; \mathbf{M}) \\ & \left. + 2(\xi s + (\tilde{\xi} - \xi X)t)C_0(0, 0, t; \mathbf{M}) - 2(\xi(1+X) - \tilde{\xi})sC_0(0, 0, s; \mathbf{M}) - \xi \frac{s}{M^2} \right], \quad (3.6) \end{aligned}$$

where  $C_0$  and  $D_0$  are scalar Passarino-Veltman functions, and we adopt the notation  $\mathbf{M} \equiv (M, M, M)$  and  $\mathbf{M} \equiv (M, M, M, M)$  in the arguments of  $C_0$  and  $D_0$ , respectively. The convention on the arguments of the scalar functions follows Ref. [19]. The form factors  $\mathcal{F}'$  and  $\mathcal{D}'$  are simply obtained from the above expressions upon the substitution  $\text{Re}[\lambda_L^I(\lambda_E^I)^*A] \rightarrow i\text{Im}[\lambda_L^I(\lambda_E^I)^*A]$ .

In order to compare the above results with those obtained with the EFT approach (see Sec. 3.2), we perform a power expansion in  $\sqrt{s}/M \ll 1$ ,

$$\begin{aligned} \mathcal{D} \simeq & \frac{ie\text{Re}[\lambda_L^I(\lambda_E^I)^*A]}{192\sqrt{2}\pi^2M^3} \left\{ \left[ \xi(1+2X) - 2\tilde{\xi} \right] - \frac{1}{15} \left[ \xi(1+3X) - 3\tilde{\xi} \right] \frac{s}{M^2} \right. \\ & \left. + \frac{1}{280} \left[ (\xi(3+8X) - 8\tilde{\xi}_{eW}) - 6\frac{tu}{s^2} (\xi(1+2X) - 2\tilde{\xi}) \right] \frac{s^2}{M^4} + \mathcal{O}\left(\frac{s^3}{M^6}\right) \right\}, \quad (3.7) \end{aligned}$$

$$\mathcal{F} \simeq \frac{ie\text{Re}[\lambda_L^I(\lambda_E^I)^*A]}{192\sqrt{2}\pi^2M^3} \left\{ \frac{1}{30} \left[ \xi(1+3X) - 3\tilde{\xi} \right] \frac{s}{M^2} + \frac{\xi}{280} \frac{s^2}{M^4} + \mathcal{O}\left(\frac{s^3}{M^6}\right) \right\}. \quad (3.8)$$

A few comments on the above expressions are in order: *i*) at  $d=6$  level, only the first term of the form factor  $\mathcal{D}^{(\prime)}$  survives and it precisely reproduces the EFT result, see Eq. (3.13) in the following section; *ii*) higher order terms are highly suppressed by small numerical coefficients making the EFT result quite accurate even for  $\sqrt{s} \sim M$ . This finding is rather unexpected, since in most cases the breakdown of the EFT description quickly arises as the energy  $\sqrt{s}$  approaches the EFT cutoff.

**Model II:** In the case of the simplified model II, we follow the same procedure outlined above. The resulting analytical expressions for the form factors read,

$$\begin{aligned} \mathcal{D} = & \frac{ieM^2 \text{Re}[\lambda_L^{\text{II}}(\lambda_E^{\text{II}})^* \kappa]}{32\sqrt{2}\pi^2 stu} \left[ -2u \left( 2\xi s + (\xi X - \tilde{\xi}) \frac{t^2}{M^2} \right) C_0(0, 0, t; \mathbf{M}) \right. \\ & - 2t \left( 2\xi s + (\xi X - \tilde{\xi}) \frac{u^2}{M^2} \right) C_0(0, 0, u; \mathbf{M}) - 2\xi \frac{st}{M^2} \Lambda(u, \mathbf{M}) - 2\xi \frac{su}{M^2} \Lambda(t; \mathbf{M}) \\ & \left. + (\xi X - \tilde{\xi}) tu \left( 4s + \frac{tu}{M^2} \right) D_0(0, 0, 0, 0, u, t; \mathbf{M}) + 6\xi \frac{s^2}{M^2} \right], \end{aligned} \quad (3.9)$$

$$\begin{aligned} \mathcal{F} = & - \frac{ieM^2 \text{Re}[\lambda_L^{\text{II}}(\lambda_E^{\text{II}})^* \kappa]}{32\sqrt{2}\pi^2 stu} \left[ -4s^2 \left( \xi(1 + X) - \tilde{\xi} \right) C_0(0, 0, s; \mathbf{M}) \right. \\ & + 2 \left( 2s(\xi s - (\xi X - \tilde{\xi})t) - \frac{ut^2}{M^2} X \right) C_0(0, 0, t; \mathbf{M}) \\ & + 2 \left( 2s(\xi s - (\xi X - \tilde{\xi})u) - \frac{u^2 t}{M^2} X \right) C_0(0, 0, u; \mathbf{M}) - 2 \left( \xi(1 + X) - \tilde{\xi} \right) st^2 D_0(0, s, 0, t, 0, 0; \mathbf{M}) \\ & - 2 \left( \xi(1 + X) - \tilde{\xi} \right) su^2 D_0(0, s, 0, u, 0, 0; \mathbf{M}) + \left( \xi X - \tilde{\xi} \right) tu \left( \frac{tu}{M^2} + 4s \right) D_0(0, 0, 0, 0, u, t; \mathbf{M}) \\ & \left. - 2\xi \frac{st}{M^2} \Lambda(u; \mathbf{M}) - 2\xi \frac{su}{M^2} \Lambda(t; \mathbf{M}) + 6\xi \frac{s^2}{M^2} \right], \end{aligned} \quad (3.10)$$

where  $\Lambda(x, M_1, M_2)$  is the part of the Passarino-Veltman  $B_0$  function containing the  $x$  plane branch cut [19]. Again, the form factors for the  $\gamma^5$  terms are identical upon the substitution  $\text{Re}[\lambda_L^{\text{II}}(\lambda_E^{\text{II}})^* \kappa] \rightarrow i\text{Im}[\lambda_L^{\text{II}}(\lambda_E^{\text{II}})^* \kappa]$ .

The low-energy expansion  $\sqrt{s}/M \ll 1$  of the form-factors given above reads

$$\begin{aligned} \mathcal{D} \simeq & - \frac{ie \text{Re}[\lambda_L^{\text{II}}(\lambda_E^{\text{II}})^* \kappa]}{96\sqrt{2}\pi^2 M^2} \left\{ \left[ \xi(1 + X) - \tilde{\xi} \right] - \frac{1}{60} \left[ \xi(2 + 3X) - 3\tilde{\xi} \right] \frac{s}{M^2} \right. \\ & \left. + \frac{1}{840} \left[ (\xi(3 + 4X) - 4\tilde{\xi}) - 6(\xi(1 + X) - \tilde{\xi}) \frac{tu}{s^2} \right] \frac{s^2}{M^4} + \mathcal{O} \left( \frac{s^3}{M^6} \right) \right\}, \end{aligned} \quad (3.11)$$

$$\begin{aligned} \mathcal{F} \simeq & - \frac{ie \text{Re}[\lambda_L^{\text{II}}(\lambda_E^{\text{II}})^* \kappa]}{96\sqrt{2}\pi^2 M^2} \left\{ \frac{1}{60} \left[ \xi(8 + 9X) - 9\tilde{\xi} \right] \frac{s}{M^2} + \frac{1}{840} \left[ \xi(15 + 14X) - 14\tilde{\xi} \right] \frac{s^2}{M^4} + \mathcal{O} \left( \frac{s^3}{M^6} \right) \right\}. \end{aligned} \quad (3.12)$$

As before, the EFT amplitude is correctly reproduced and the sub-leading power corrections are suppressed by large numerical factors.

### 3.2 $\mu^+ \mu^- \rightarrow h\gamma$ in EFT

Before presenting our numerical results, we remind the reader of the EFT description of the  $\mu^+ \mu^- \rightarrow h\gamma$  process. To this purpose, we assume that the center-of-mass energy  $\sqrt{s}$  is much larger than the masses involved in this process, but still sufficiently smaller than the EFT cutoff. In this case, the  $\mu^+ \mu^- \rightarrow h\gamma$  scattering is dominated by a single  $d = 6$  operator,  $\mathcal{O}_{e\gamma} = \bar{\ell} \sigma^{\mu\nu} e H F_{\mu\nu}$ , which is a linear combination of the operators defined in Eq. (2.3).

The EFT contribution to the  $\mu^+ \mu^- \rightarrow h\gamma$  amplitude is encapsulated in the form-factors  $\mathcal{D}^{(\prime)}$ ,

$$\mathcal{D}_{\text{EFT}} = -i\sqrt{2} \text{Re}(C_{e\gamma}), \quad \mathcal{D}'_{\text{EFT}} = \sqrt{2} \text{Im}(C_{e\gamma}), \quad (3.13)$$



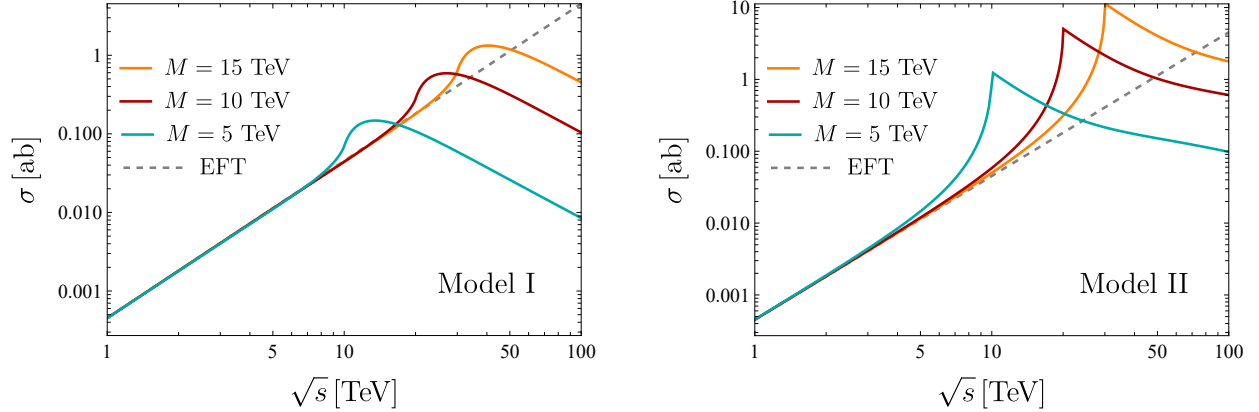


Figure 4: Left (right): Cross-section of  $\mu^+\mu^- \rightarrow h\gamma$  for  $M = (5, 10, 15)$  TeV and  $X = 1/2$  for the simplified model I (II) in the representation  $R = 121$  (see Appendix A). The NP couplings have been fixed to solve the  $(g - 2)_\mu$  discrepancy. The dashed lines correspond to the EFT prediction.

whereas  $\mathcal{F}^{(\prime)} = 0$  at this order in the EFT expansion. By using the effective coefficients  $C_{e\gamma}$  given in Eq. (2.5)–(2.6) for the simplified models I and II, respectively, we retrieve the first term in the  $s/M$  power expansion of  $\mathcal{D}^{(\prime)}$  in Sec. 3.1, which is an important cross-check of our results. After integrating over  $t$ , the total  $\mu^+\mu^- \rightarrow h\gamma$  cross-section reads

$$\sigma_{h\gamma}^{\text{EFT}} = \frac{s |C_{e\gamma}|^2}{48\pi} \approx 0.7 \text{ ab} \left( \frac{\sqrt{s}}{30 \text{ TeV}} \right)^2 \left( \frac{\Delta a_\mu}{3 \times 10^{-9}} \right)^2. \quad (3.14)$$

in agreement with Ref. [11]. It is clear from this equation that the sensitivity on  $\Delta a_\mu$  increases with  $\sqrt{s}$ , as long as the EFT approach is valid. The energy scale  $\sqrt{s}$  at which the total cross-section departs from the EFT predictions for a given mass  $M$  of the NP states will be derived along with our numerical results in the following section.

In principle, the operator  $\mathcal{O}_{eH} = (H^\dagger H) \bar{\ell} e H$  would also contribute to the  $\mu^+\mu^- \rightarrow h\gamma$  process via a modification of the Higgs couplings to muons. However, this effect scales as  $\sigma \propto 1/s$  and, therefore, it is safely negligible at high-energies compared to the NP contributions discussed above. Interestingly,  $\mathcal{O}_{eH}$  also contributes to the processes  $\mu^+\mu^- \rightarrow hh$  and  $\mu^+\mu^- \rightarrow hhh$ . In particular, we find that the cross-section of  $\mu^+\mu^- \rightarrow hh$  is independent of the collider energy, whereas the one of  $\mu^+\mu^- \rightarrow hhh$  grows linearly with  $s$  and it has a comparable size to the  $\mu^+\mu^- \rightarrow h\gamma$  cross-section. However, in order to determine the NP sensitivity of  $\mu^+\mu^- \rightarrow hh(h)$ , a detailed study of the SM background [20] is mandatory, which is beyond the scope of the present paper.<sup>5</sup>

### 3.3 Numerical results

First, we report in Fig. 4 the total cross section of  $\mu^+\mu^- \rightarrow h\gamma$  as a function of  $\sqrt{s}$  for the simplified models I (left panel) and II (right panel), with the representation  $R = 121$  and hypercharge  $X = 1/2$  taken as our benchmark. The masses of the new states are fixed to three reference values, namely  $M = (5, 10, 15)$  TeV, and the NP couplings are fixed to solve the  $(g - 2)_\mu$  discrepancy. Interestingly, we confirm numerically that the EFT agrees with the UV theory remarkably well for energies as

<sup>5</sup>Note, also, that the dependence of the Wilson coefficient of  $\mathcal{O}_{eH}$  on the NP couplings differs from the one of  $C_{e\gamma}$  by a factor of  $(A/M)^2$  (model I) or  $\kappa^2$  (model II), thus not being in direct correspondence with  $\Delta a_\mu$ .

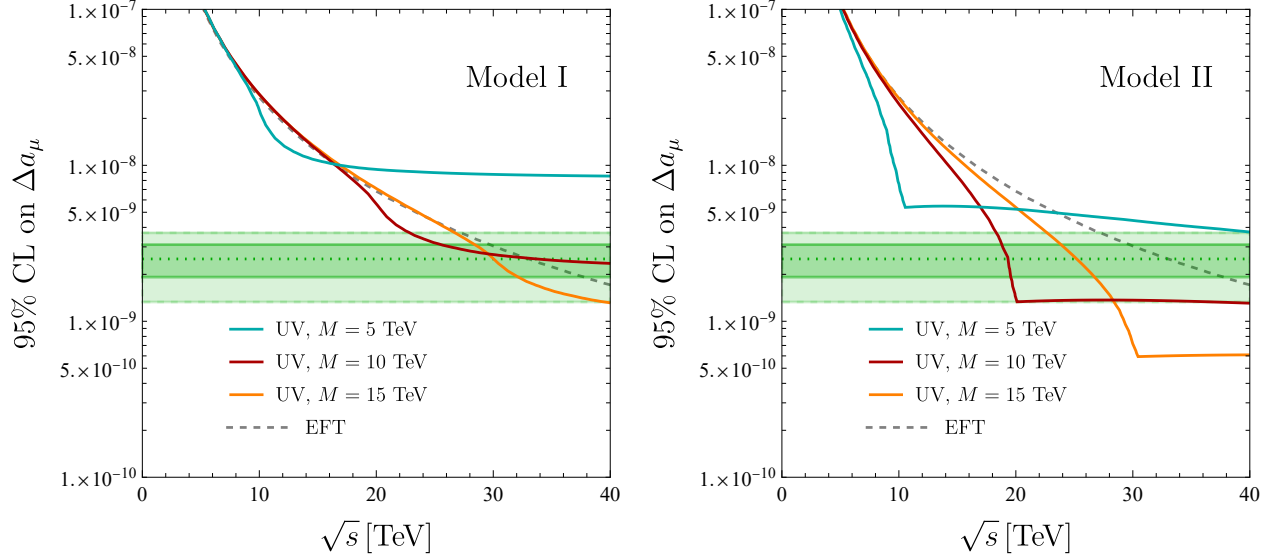


Figure 5: 95% C.L. reach on  $\Delta a_\mu$  as a function of the center-of-mass energy  $\sqrt{s}$  from the process  $\mu^+\mu^- \rightarrow h\gamma$  in EFT (dashed line) and in the simplified models I (left) and II (right) for three reference NP masses  $M = (5, 10, 15)$  TeV and for the hypercharge  $X = 1/2$ .

large as  $\sqrt{s} \sim M$  in both scenarios. At  $\sqrt{s} \sim 2M$ , the UV cross-section shows a resonance peak corresponding to the fact that the virtual particles can then be produced on-shell. Finally, for energies  $\sqrt{s} \gtrsim 2M$  the UV cross-section scales as  $1/s$ , as expected by the unitarity of the  $S$ -matrix. The most prominent difference between the two models is that in the model II the resonance is larger and more peaked than in the model I.

Next, following the analysis of Ref. [11], we study the capability of the process  $\mu^+\mu^- \rightarrow h\gamma$  to probe the muon  $g-2$  anomaly. The SM irreducible  $\mu^+\mu^- \rightarrow h\gamma$  background is small and can be neglected for  $\sqrt{s} \gg 1$  TeV. Instead, the main source of background comes from the  $\mu^+\mu^- \rightarrow Z\gamma$  process, where the  $Z$  boson is mis-reconstructed as a Higgs boson. An efficient way to isolate the  $h\gamma$  signal from the background is to exploit the different angular distributions of the two processes, requiring that the probability of mis-reconstructing a  $Z$  boson as a Higgs is less than 10%.

In Fig. 5, we show the 95% C.L. reach from  $\mu^+\mu^- \rightarrow h\gamma$  on the anomalous magnetic moment of the muon as a function of the center-of-mass energy  $\sqrt{s}$  for the simplified model I (left panel) and II (right panel), and for three reference NP masses  $M = (5, 10, 15)$  TeV. The dashed lines correspond to the EFT limit derived from Eq. (3.14). The NP sensitivity has been obtained imposing that the significance of the signal satisfy  $S > 2$ , where  $S = N_S/\sqrt{N_B + N_S}$ , and  $N_S$  and  $N_B$  denote the number of signal and background events, respectively. The number of events is estimated considering a  $b\bar{b}$  final state, with an 80%  $b$ -tagging efficiency and by imposing the kinematical cut  $|\cos\theta| < 0.6$  for which  $S$  is maximized, where  $\theta$  denotes the photon scattering-angle.

As already discussed above, the EFT result is accurately reproduced for  $\sqrt{s} \lesssim M$ . On the other hand, for energies close to the resonant-production threshold, i.e.  $\sqrt{s} = 2M$ , the simplified models have an even higher sensitivity to  $\Delta a_\mu$  than the EFT, especially in the case of the model II. Finally, for energies  $\sqrt{s} \gg 2M$ , the  $\mu^+\mu^- \rightarrow h\gamma$  cross-section in the simplified models scales as  $\sigma \sim 1/s$  and therefore the number of signal events  $N_S \propto \sigma \times \mathcal{L}$  becomes constant with respect to the energy, since the luminosity scales as  $\mathcal{L} \propto s$  [12]. This behaviour is in contrast with the EFT expectation, for which  $\sigma \sim s$  and therefore  $N_S \propto s^2$ .

As shown by our analysis, the capability of the process  $\mu^+\mu^- \rightarrow h\gamma$  to probe NP effects in  $\Delta a_\mu$  within an EFT framework [11] is confirmed and reinforced also in explicit simplified models.

## 4 Direct high-energy probes of the muon $g - 2$

In this section, we will analyse the capability of a high-energy muon collider to discover the new particles of the simplified models I and II via their direct production. In particular, since we assume an underlying  $Z_2$  symmetry, the new states are always produced in pairs. Since the muon  $g-2$  anomaly can be typically accommodated for  $M \lesssim 15$  TeV, it follows that a high-energy muon collider running with energies  $\sqrt{s} \gtrsim 30$  TeV should be able to directly observe these new particles.

### 4.1 $2 \rightarrow 2$ processes

The most relevant  $2 \rightarrow 2$  processes are schematically represented by the Feynman diagrams of Fig. 6, where  $\Phi, \Psi$  refer collectively to the scalar and fermion fields of the models I or II. In the following, we report the analytical expressions of the relevant cross sections.



Figure 6: Feynman diagrams for  $2 \rightarrow 2$  pair production processes in the simplified models I and II.

For the model I, we obtain

$$\begin{aligned}
 \sigma(\mu^+\mu^- \rightarrow \bar{\Phi}_i\Phi_i) &= \frac{\eta |\lambda_i^I|^4}{32\pi s} \left[ \tanh^{-1} \left( \sqrt{1 - \frac{4M^2}{s}} \right) - \sqrt{1 - \frac{4M^2}{s}} \right], \\
 \sigma(\mu^+\mu^- \rightarrow \bar{\Phi}_i\Phi_j) &= \frac{\eta |\lambda_i^I\lambda_j^I|^2}{64\pi s} \sqrt{1 - \frac{4M^2}{s}}, \\
 \sigma(\mu^+\mu^- \rightarrow \bar{\Psi}\Psi) &= \frac{|\lambda_E^I|^4 + \eta |\lambda_L^I|^4}{64\pi s} \sqrt{1 - \frac{4M^2}{s}},
 \end{aligned} \tag{4.1}$$

whereas for the model II

$$\begin{aligned}
 \sigma(\mu^+\mu^- \rightarrow \bar{\Psi}_i\Psi_i) &= \frac{\eta |\lambda_i^{II}|^4}{64\pi s} \sqrt{1 - \frac{4M^2}{s}}, \\
 \sigma(\mu^+\mu^- \rightarrow \bar{\Psi}_i\Psi_j) &= \frac{\eta |\lambda_i^{II}\lambda_j^{II}|^2}{64\pi s} \sqrt{1 - \frac{4M^2}{s}}, \\
 \sigma(\mu^+\mu^- \rightarrow \bar{\Phi}\Phi) &= \frac{|\lambda_E^{II}|^4 + \eta |\lambda_L^{II}|^4}{32\pi s} \left[ \tanh^{-1} \left( \sqrt{1 - \frac{4M^2}{s}} \right) - \sqrt{1 - \frac{4M^2}{s}} \right],
 \end{aligned} \tag{4.2}$$

where  $i, j \in \{E, L\}$ ,  $i \neq j$  and the factor  $\eta$  is equal to 1 for the representations  $R = \{121, 212\}$ , while  $\eta = 1$  or 4 for  $R = \{323, 232\}$  depending on the specific final state<sup>6</sup>. For the reference values  $\sqrt{s} = 30$  TeV and  $M = 10$  TeV, the above cross-sections attain comparable values of order  $10^4$  ab. Note that in Eqs. (4.1) and (4.2), we have neglected the contributions stemming from the s-channel exchange of the SM gauge bosons  $\gamma$  and  $Z$ . Indeed, since the solution of the muon  $g-2$  anomaly requires  $\lambda_{E,L} \gtrsim 2$ , the t-channel diagrams of Fig. 6 are by far dominant.

## 4.2 $2 \rightarrow 3$ processes

Although the  $2 \rightarrow 2$  processes shown in Fig. 6 are unavoidably induced once a NP contribution to the muon  $g-2$  is generated, it is important to stress that their observation cannot be promoted by any means as an unambiguous test of the  $\Delta a_\mu$  anomaly. Indeed,  $\Delta a_\mu$  and the cross-sections in Eq. (4.1) and (4.2) depend on different combinations of the simplified models parameters. Therefore, it would be desirable to identify high-energy processes (if any) that are in one-to-one correspondence with the NP effects entering the muon  $g-2$ . Interestingly, such processes do exist and are given by  $\mu^+\mu^- \rightarrow h\bar{\Psi}\Psi$  in model I and by  $\mu^+\mu^- \rightarrow h\bar{\Phi}\Phi$  in model II, as illustrated in Fig. 7.<sup>7</sup> The correspondence is evident by comparing this diagram with the one for  $\Delta a_\mu$  depicted in Fig. 1.

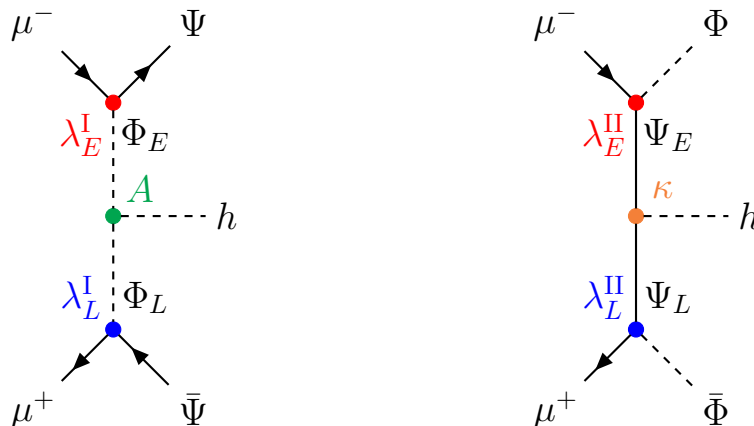


Figure 7: Feynman diagrams contributing to the direct production channels  $\mu^+\mu^- \rightarrow h\bar{\Psi}\Psi, h\bar{\Phi}\Phi$  in the simplified models I (left) and II (right).

The differential cross-sections for these processes can be written in the following form,

$$d\sigma_{2 \rightarrow 3} = \frac{|\bar{\mathcal{A}}|^2}{256\pi^3} \frac{\lambda^{1/2}(s, 0, q^2)\lambda^{1/2}(q^2, M^2, M^2)}{s^2 q^2} \frac{d \cos \theta_1}{2} \frac{d\varphi_1}{2\pi} \frac{d \cos \theta_2}{2} \frac{d\varphi_2}{2\pi} dq^2 \quad (4.3)$$

where  $\lambda(x, y, z) = x^2 + y^2 + z^2 - 2(xy + xz + yz)$  is the Källén function, and we define  $q = k_1 + k_2$ , with  $q^2 \in [4M^2, s]$ . The angles  $\theta_i$  and  $\varphi_i$  are defined in Fig. 9 and are integrated in the ranges  $\theta_i \in [0, \pi]$

<sup>6</sup>In the presence of an  $SU(2)_L$  triplet  $\chi^a$  ( $a = 1, 2, 3$ ), the electric charge eigenstates are  $\chi_\pm = \frac{\chi^1 \mp i\chi^2}{\sqrt{2}}$  and  $\chi_3$ . Then, in the model I,  $\eta = 4$  for the final states  $(\bar{\Psi} - \Psi_-), (\bar{\Phi}_{L, \frac{1}{2}} \Phi_{L, \frac{1}{2}}), (\bar{\Phi}_{L, \frac{1}{2}} \Phi_{E, +}), (\Phi_{L, \frac{1}{2}} \bar{\Phi}_{E, +})$  of the representation  $R = 323$ , and  $(\bar{\Psi}_{\frac{1}{2}} \Psi_{\frac{1}{2}}), (\bar{\Phi}_{L, -} \Phi_{L, -}), (\bar{\Phi}_{L, -} \Phi_{E, -\frac{1}{2}}), (\Phi_{L, -} \bar{\Phi}_{E, -\frac{1}{2}})$  for  $R = 232$ . In all other cases  $\eta = 1$ . The lower index  $\pm \frac{1}{2}$  refers to the component of the isospin doublets. For model II the situation is completely analogous.

<sup>7</sup>Other possibilities are given by  $\mu^+\mu^- \rightarrow h\bar{\Phi}_{E(L)}\Phi_{E(L)}$  in model I and  $\mu^+\mu^- \rightarrow h\bar{\Psi}_{E(L)}\Psi_{E(L)}$  in model II, where the Higgs is emitted from the final state legs. Instead, the analogous processes  $\mu^+\mu^- \rightarrow h\bar{\Phi}_{E(L)}\Phi_{L(E)}$  and  $\mu^+\mu^- \rightarrow h\bar{\Psi}_{E(L)}\Psi_{L(E)}$  do not depend on the same combination of NP couplings as  $\Delta a_\mu$ . A careful analysis of the different final state products and of the Higgs kinematical properties may be exploited to disentangle these processes.

and  $\varphi_i \in [0, 2\pi]$ . For a detailed discussion about the non-trivial kinematics of  $2 \rightarrow 3$  processes we refer to appendix B. The  $|\overline{\mathcal{A}}|^2$  expression for the process  $\mu^+(p_b)\mu^-(p_a) \rightarrow h(k)\bar{\Psi}(k_2)\Psi(k_1)$  in the model I reads<sup>8</sup>

$$|\overline{\mathcal{A}}|^2 = \frac{\eta}{4} \frac{|\lambda_L^I \lambda_E^I A|^2}{[M^2 - (p_a - k_1)^2][M^2 - (p_b - k_2)^2]}. \quad (4.4)$$

Similarly, the squared amplitude  $\mu^+(p_b)\mu^-(p_a) \rightarrow h(k)\bar{\Phi}(k_2)\Phi(k_1)$  in the model II is given by

$$|\overline{\mathcal{A}}|^2 = \frac{2\eta|\lambda_L^{\text{II}}\lambda_E^{\text{II}}\kappa|^2 M^2}{[M^2 - (p_a - k_1)^2]^2[M^2 - (p_b - k_2)^2]^2} \left[ p_a \cdot (k_2 - k_1) p_b \cdot (k_1 - k_2) - 2 \left( p_a \cdot k_1 p_b \cdot k_2 - \frac{sM^2}{4} \right) \left( 1 - \frac{k_1 \cdot k_2}{2M^2} \right) \right], \quad (4.5)$$

where the scalar products can be easily computed by using the expressions from appendix B.

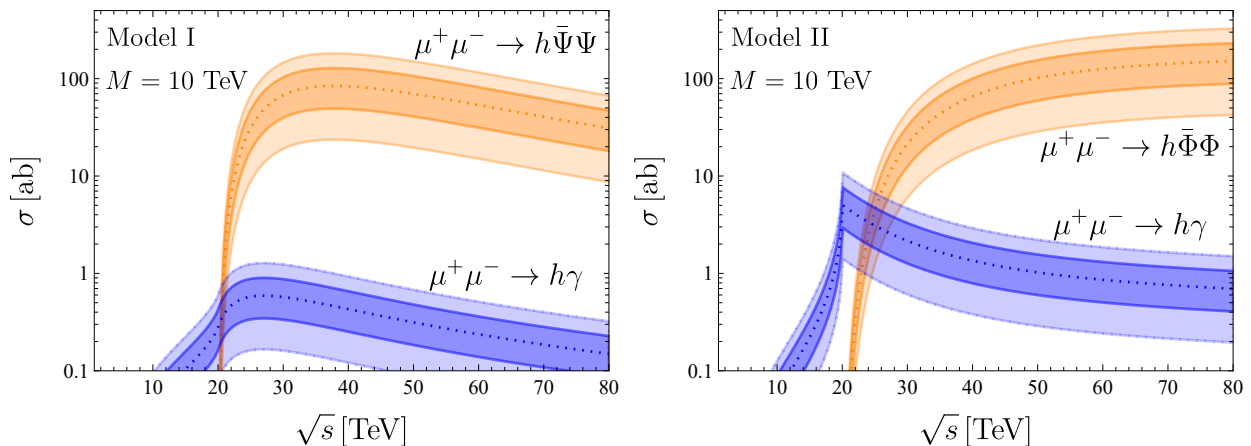


Figure 8: Cross-sections of  $\mu^+\mu^- \rightarrow h\gamma$  and  $\mu^+\mu^- \rightarrow h\bar{\Psi}\Psi, h\bar{\Phi}\Phi$  vs.  $\sqrt{s}$  setting  $X = 1/2$  and  $M = 10$  TeV in the simplified model I (left) and II (right). Inner (outer) regions correspond to  $\Delta a_\mu$  values in the  $1\sigma$  ( $2\sigma$ ) allowed range.

In Fig. 8, we report the cross-sections of  $\mu^+\mu^- \rightarrow h\bar{\Psi}\Psi, h\bar{\Phi}\Phi$  vs.  $\sqrt{s}$  setting  $X = 1/2$  and  $M = 10$  TeV. Inner (outer) regions correspond to  $\Delta a_\mu$  values in the  $1\sigma$  ( $2\sigma$ ) allowed range. As expected, the  $2 \rightarrow 3$  cross-sections are typically 2-3 orders of magnitude smaller than those for  $2 \rightarrow 2$  processes (see Eqs. (4.1) and (4.2)) due to the additional phase-space suppression. However, at a muon collider running at  $\sqrt{s} = 30$  TeV, we expect several hundreds of events for these  $2 \rightarrow 3$  processes that can be discriminated from the background thanks to the coincidence of two NP particles accompanied by a Higgs boson. In Fig. 8, we also plot the cross-section of  $\mu^+\mu^- \rightarrow h\gamma$  as a function of  $\sqrt{s}$  to stress its interplay with the direct search processes  $\mu^+\mu^- \rightarrow h\bar{\Psi}\Psi$  and  $\mu^+\mu^- \rightarrow h\bar{\Phi}\Phi$ . Indeed, for collider energies below the threshold required for a direct production of new states,  $\mu^+\mu^- \rightarrow h\gamma$  provides a unique way to test the muon  $g-2$  anomaly. Instead, when the final states  $h\bar{\Psi}\Psi$  and  $h\bar{\Phi}\Phi$  are kinematically allowed, the study of their correlation with the process  $\mu^+\mu^- \rightarrow h\gamma$  would still be of great importance to pin down the details of the underlying NP model.

<sup>8</sup>In this case,  $\eta = 4$  for  $\mu^+\mu^- \rightarrow h\bar{\Psi}_-\Psi_-$  ( $R = 323$ ) and  $\mu^+\mu^- \rightarrow h\bar{\Psi}_{\frac{1}{2}}\Psi_{\frac{1}{2}}$  ( $R = 232$ ), while  $\eta = 1$  otherwise.

## 5 Conclusions

In this paper, we have studied the solution of the muon  $g-2$  anomaly through new physics scenarios with heavy scalars and vector-like fermions appearing above the TeV-scale. Such a solution is only viable provided that a chiral enhancement is at work, which in turn requires that the new states couple to the SM Higgs boson. As already emphasised in the EFT context, a muon collider running at center-of-mass energies  $\sqrt{s}$  in the multi-TeV range would be the ideal machine to test this anomaly model-independently through the study of the  $\mu^+\mu^- \rightarrow h\gamma$  process [11].

We have explored the connection between  $\Delta a_\mu$  and  $\mu^+\mu^- \rightarrow h\gamma$  in the context of the concrete NP scenarios mentioned above, which contribute to both observables at one-loop level, extending the EFT results to the case where  $\sqrt{s}$  is larger than the mass of the new particles. In particular, we have found that the EFT approach describes remarkably well the  $\mu^+\mu^- \rightarrow h\gamma$  cross-section for  $\sqrt{s}$  values even at the vicinity of the EFT cutoff, where the EFT description is expected to break down, as shown in Figs. 4 and 5. These results confirm and reinforce the complementarity of  $\Delta a_\mu$  with the high-energy process  $\mu^+\mu^- \rightarrow h\gamma$ .

Another goal of this work has been to study the direct search signatures of our simplified models, as well as their interplay with the indirect search  $\mu^+\mu^- \rightarrow h\gamma$ . If kinematically allowed, the processes  $\mu^+\mu^- \rightarrow \bar{\Psi}\Psi, \bar{\Phi}\Phi$ , where  $\Psi$  and  $\Phi$  refer to heavy vector-like fermions and scalars, are unavoidably induced with sizable cross-sections. However, the cross-sections of these  $2 \rightarrow 2$  processes are not directly correlated with  $\Delta a_\mu$  as they depend on different combinations of NP couplings.

We have shown in this paper that the cross-sections of the processes  $\mu^+\mu^- \rightarrow h\bar{\Psi}\Psi, h\bar{\Phi}\Phi$  with a Higgs boson in the final state, which we have computed in full generality, are in one-to-one correspondence with the NP effects entering the muon  $g-2$ , as shown in Fig. 1 and 7. Although suppressed by two orders of magnitude compared to the  $2 \rightarrow 2$  processes, due to the additional phase-space suppression, we still expect several hundreds of events for  $\mu^+\mu^- \rightarrow h\bar{\Psi}\Psi, h\bar{\Phi}\Phi$  at a muon collider running at  $\sqrt{s} = 30$  TeV, which can be discriminated thanks to the coincidence of two NP particles together with a Higgs boson in the final state. As shown in Fig. 8, there is an interesting interplay between the indirect probe  $\mu^+\mu^- \rightarrow h\gamma$  and the direct ones  $\mu^+\mu^- \rightarrow h\bar{\Psi}\Psi$  and  $\mu^+\mu^- \rightarrow h\bar{\Phi}\Phi$ . Indeed, for collider energies below the threshold required for a direct production of new states,  $\mu^+\mu^- \rightarrow h\gamma$  provides a unique way to access the muon  $g-2$  anomaly. Instead, when  $\mu^+\mu^- \rightarrow h\bar{\Psi}\Psi$  and  $\mu^+\mu^- \rightarrow h\bar{\Phi}\Phi$  are kinematically allowed, they are typically the best probe of  $\Delta a_\mu$ . This complementarity illustrates the fact that a correlated study of direct and indirect new physics signals at a muon collider would be a powerful handle to disentangle among the underlying model accommodating the  $\Delta a_\mu$  anomaly.

## 6 Acknowledgments

We thank A. Wulzer for useful discussions. This project has received support from the European Union's Horizon 2020 research and innovation programme under the Marie Skłodowska-Curie grant agreement No 860881-HIDDeN.

## A Simplified model Lagrangians and RGEs

In this appendix, we collect the relevant expressions for the running of the fundamental parameters of the simplified models I and II introduced in section I. Assuming a  $Z_2$  symmetry to avoid mixing of the new states with SM fields and allowing  $SU(2)_L$  representations up to triplets, the most generic Lagrangians are [13]:

$$\begin{aligned}
\mathcal{L}_I^{121} &= \lambda_L^I \bar{\ell}^a \Psi \Phi_L^a + \lambda_E^I \bar{e} \Psi \Phi_E + A \Phi_L^{a\dagger} \Phi_E H^a + \text{h.c.}, \\
\mathcal{L}_{II}^{121} &= \lambda_L^{II} \bar{\ell}^a \Phi \Psi_L^a + \lambda_E^{II} \bar{e} \Psi_E \Phi + \kappa \bar{\Psi}_L^a \Psi_E H^a + \text{h.c.} \\
\mathcal{L}_I^{212} &= \lambda_L^I \bar{\ell}^a \Phi_L \Psi^a + \lambda_E^I \bar{e} \Psi^a (i\tau_2 \Phi_E)^a + A (i\tau_2 H)^a \Phi_L^\dagger \Phi_E^a + \text{h.c.} \\
\mathcal{L}_{II}^{212} &= \lambda_L^{II} \bar{\ell}^a \Psi_L \Phi^a + \lambda_E^{II} \bar{e} (i\tau_2 \Psi_E)^a \Phi^a + \kappa \bar{\Psi}_L (i\tau_2 H)^a \Psi_E^a + \text{h.c.} \\
\mathcal{L}_I^{323} &= \lambda_L^I \bar{\ell}^a (\tau \cdot \Psi)_{ab} \Phi_L^b + \lambda_E^I \bar{e} \Psi^\alpha \Phi_E^\alpha + A \Phi_L^{a\dagger} (\tau \cdot \Phi_E)_{ab} H^b + \text{h.c.} \\
\mathcal{L}_{II}^{323} &= \lambda_L^{II} \bar{\ell}^a (\tau \cdot \Phi)_{ab} \Psi_L^b + \lambda_E^{II} \bar{e} \Psi_E^\alpha \Phi^\alpha + \kappa \bar{\Psi}_L^a (\tau \cdot \Psi_E)_{ab} H^b + \text{h.c.} \\
\mathcal{L}_I^{232} &= \lambda_L^I \bar{\ell}^a (\tau \cdot \Phi_L)_{ab} \Psi^b + \lambda_E^I \bar{e} \Psi^a (i\tau_2 \Phi_E)^a + A (i\tau_2 H)^a (\tau \cdot \Phi_L^\dagger)_{ab} \Phi_E^b + \text{h.c.} \\
\mathcal{L}_{II}^{232} &= \lambda_L^{II} \bar{\ell}^a (\tau \cdot \Psi_L)_{ab} \Phi^b + \lambda_E^{II} \bar{e} (i\tau_2 \Psi_E)^a \Phi^a + \kappa (\tau \cdot \bar{\Psi}_L)_{ab} (i\tau_2 H)^a \Psi_E^b + \text{h.c.}
\end{aligned} \tag{A.1}$$

where  $a, b$  denote  $SU(2)_L$  indices,  $\tau$  are the Pauli matrices and the charges of the various fields are defined in Table 1.

The RGEs for the simplified model Yukawa-couplings and for the SM gauge couplings, as well as for the Higgs boson quartic coupling in the models of type-II<sup>9</sup>, have been calculated using the tool `RGBeta` [18]. They read

$$\text{Model I: } \begin{cases} (4\pi)^2 \frac{dg^2}{d \log \mu} = \beta_g g^4 \\ (4\pi)^2 \frac{dg'^2}{d \log \mu} = \beta_{g'} g'^4 \\ (4\pi)^2 \frac{d\lambda_L^I}{d \log \mu} = \lambda_L^I \left[ -\beta_L^g g^2 - \beta_L^{g'} g'^2 + \beta_L^L \lambda_L^{I2} + \beta_L^y y_\mu^2 \right] \\ (4\pi)^2 \frac{d\lambda_E^I}{d \log \mu} = \lambda_E^I \left[ -\beta_E^g g^2 - \beta_E^{g'} g'^2 + \beta_E^E \lambda_E^{I2} + \beta_E^y y_\mu^2 \right] \end{cases}, \tag{A.2}$$

$$\text{Model II: } \begin{cases} (4\pi)^2 \frac{dg^2}{d \log \mu} = \beta_g g^4 \\ (4\pi)^2 \frac{dg'^2}{d \log \mu} = \beta_{g'} g'^4 \\ (4\pi)^2 \frac{d\lambda_L^{II}}{d \log \mu} = \lambda_L^{II} \left[ -\beta_L^g g^2 - \beta_L^{g'} g'^2 + \beta_L^L \lambda_L^{II2} + \beta_L^E \lambda_E^{II2} + \beta_L^\kappa \kappa^2 + \beta_L^y y_\mu^2 \right] + \beta_L^{yE\kappa} y_\mu \lambda_E^{II} \kappa \\ (4\pi)^2 \frac{d\lambda_E^{II}}{d \log \mu} = \lambda_E^{II} \left[ -\beta_E^g g^2 - \beta_E^{g'} g'^2 + \beta_E^L \lambda_L^{II2} + \beta_E^E \lambda_E^{II2} + \beta_E^\kappa \kappa^2 + \beta_E^y y_\mu^2 \right] + \beta_E^{yL\kappa} y_\mu \lambda_L^{II} \kappa \\ (4\pi)^2 \frac{d\kappa}{d \log \mu} = \kappa \left[ -\beta_\kappa^g g^2 - \beta_\kappa^{g'} g'^2 + \beta_\kappa^L \lambda_L^{II2} + \beta_\kappa^E \lambda_E^{II2} + \beta_\kappa^\kappa \kappa^2 + \beta_\kappa^y (y_\mu^2 + 3y_t^2) \right] + \beta_\kappa^{LE} y_\mu \lambda_L^{II} \lambda_E^{II} \\ (4\pi)^2 \frac{d\lambda}{d \log \mu} = \beta_\lambda^{\text{SM}}(g, g', \lambda, y_t) + \beta_\lambda^{\lambda\kappa} \lambda \kappa^2 - \beta_\lambda^\kappa \kappa^4 \end{cases} \tag{A.3}$$

The values of the coefficients of the  $\beta$ -functions for the various representation are given in Table 3, where they are written as vectors with components ordered as they appear in Eqs. (A.2) and (A.3).

<sup>9</sup>In the models of type-I, the Higgs quartic does not receive BSM contributions at one-loop.

$R$	Model I	Model II
121	$\beta_g = \beta_g^{\text{SM}} + \frac{1}{3}$ $\beta_{g'} = \beta_{g'}^{\text{SM}} + \frac{1}{3}(3+8X+14X^2)$ $\beta_L^i = \left\{ \frac{9}{4}, \frac{3}{4}(1+4X^2), \frac{5}{2}, \frac{1}{2} \right\}$ $\beta_E^i = \{0, 3(1+X^2), 2, 1\}$	$\beta_g = \beta_g^{\text{SM}} + \frac{4}{3}$ $\beta_{g'} = \beta_{g'}^{\text{SM}} + \frac{2}{3}(6+16X+13X^2)$ $\beta_L^i = \left\{ \frac{9}{2}, \frac{3}{2}(1+2X+2X^2), 3, 1, \frac{1}{2}, \frac{1}{2}, 2 \right\}$ $\beta_E^i = \{0, 3(2+2X+X^2), 2, 2, 1, 1, 4\}$ $\beta_\kappa^i = \left\{ \frac{9}{4}, \frac{15}{4}+9X+6X^2, \frac{1}{4}, \frac{1}{4}, \frac{7}{2}, 1, 1 \right\}$ $\beta_\lambda^i = \{4, 2\}$
212	$\beta_g = \beta_g^{\text{SM}} + \frac{5}{3}$ $\beta_{g'} = \beta_{g'}^{\text{SM}} + \frac{1}{6}(9+20X+44X^2)$ $\beta_L^i = \left\{ \frac{9}{2}, \frac{3}{4}(1+4X^2), 3, \frac{1}{2} \right\}$ $\beta_E^i = \left\{ \frac{9}{4}, 3(1+X^2), \frac{5}{2}, 1 \right\}$	$\beta_g = \beta_g^{\text{SM}} + \frac{5}{3}$ $\beta_{g'} = \beta_{g'}^{\text{SM}} + \frac{2}{3}(9+20X+14X^2)$ $\beta_L^i = \left\{ \frac{9}{4}, \frac{3}{2}(1+2X+2X^2), \frac{5}{2}, 1, 1, \frac{1}{2}, -2 \right\}$ $\beta_E^i = \left\{ \frac{9}{4}, 3(2+2X+X^2), 1, \frac{5}{2}, \frac{1}{2}, 1, -2 \right\}$ $\beta_\kappa^i = \left\{ \frac{9}{4}, \frac{15}{4}+9X+6X^2, \frac{1}{2}, \frac{1}{4}, \frac{7}{2}, 1, -1 \right\}$ $\beta_\lambda^i = \{4, 2\}$
323	$\beta_g = \beta_g^{\text{SM}} + 7$ $\beta_{g'} = \beta_{g'}^{\text{SM}} + \frac{1}{3}(7+16X+34X^2)$ $\beta_L^i = \left\{ \frac{33}{4}, \frac{3}{4}(1+4X^2), \frac{11}{2}, \frac{1}{2} \right\}$ $\beta_E^i = \{6, 3(1+X^2), 3, 1\}$	$\beta_g = \beta_g^{\text{SM}} + 8$ $\beta_{g'} = \beta_{g'}^{\text{SM}} + \frac{2}{3}(14+32X+23X^2)$ $\beta_L^i = \left\{ \frac{9}{2}, \frac{3}{2}(1+2X+2X^2), 5, 1, \frac{3}{2}, \frac{1}{2}, -2 \right\}$ $\beta_E^i = \{6, 3(2+2X+X^2), 2, 3, 1, 1, -4\}$ $\beta_\kappa^i = \left\{ \frac{33}{4}, \frac{15}{4}+9X+6X^2, \frac{3}{4}, \frac{1}{4}, \frac{17}{2}, 1, -1 \right\}$ $\beta_\lambda^i = \{12, 10\}$
232	$\beta_g = \beta_g^{\text{SM}} + 3$ $\beta_{g'} = \beta_{g'}^{\text{SM}} + \frac{1}{6}(11+28X+52X^2)$ $\beta_L^i = \left\{ \frac{9}{2}, \frac{3}{4}(1+4X^2), 5, \frac{1}{2} \right\}$ $\beta_E^i = \left\{ \frac{9}{4}, 3(1+X^2), \frac{5}{2}, 1 \right\}$	$\beta_g = \beta_g^{\text{SM}} + 7$ $\beta_{g'} = \beta_{g'}^{\text{SM}} + \frac{2}{3}(11+28X+22X^2)$ $\beta_L^i = \left\{ \frac{33}{4}, \frac{3}{2}(1+2X+2X^2), \frac{11}{2}, 1, 1, \frac{1}{2}, 2 \right\}$ $\beta_E^i = \left\{ \frac{9}{4}, 3(2+2X+X^2), 3, \frac{5}{2}, \frac{3}{2}, 1, 6 \right\}$ $\beta_\kappa^i = \left\{ \frac{33}{4}, \frac{15}{4}+9X+6X^2, \frac{1}{2}, \frac{1}{4}, \frac{17}{2}, 1, 1 \right\}$ $\beta_\lambda^i = \{12, 10\}$

Table 3:  $\beta$ -function coefficients of the RGEs in Eqs. (A.2) and (A.3), where  $\beta_g^{\text{SM}} = -\frac{19}{3}$  and  $\beta_{g'}^{\text{SM}} = \frac{41}{3}$ . The upper index  $i$  of  $\beta_X^i$  refers to its components as ordered in Eqs. (A.2) and (A.3); for example, in model I,  $\beta_L^i = \{\beta_L^g, \beta_L^{g'}, \beta_L^L, \beta_L^y\}$ .



## B Kinematics of $2 \rightarrow 3$ scattering processes

As discussed in section 4, the processes  $\mu^+\mu^- \rightarrow h\bar{\Psi}\Psi$  and  $\mu^+\mu^- \rightarrow h\bar{\Phi}\Phi$  are ideal tests of the muon  $g-2$  anomaly. In this appendix, we give details about the kinematics of these processes, which are depicted in Fig. 3. The integrated cross section,

$$\sigma_{2 \rightarrow 3} = \int \frac{1}{2s} (2\pi)^4 \delta^{(4)}(p_a + p_b - k - k_1 - k_2) |\bar{\mathcal{A}}|^2 d\Phi_3, \quad (\text{B.1})$$

can be evaluated by splitting the phase-space into the product of two-body phase spaces,

$$d\Phi_3 = \int dq^2 (2\pi)^3 d\Phi_2(p_a + p_b, k, q) d\Phi_2(q, k_1, k_2), \quad (\text{B.2})$$

corresponding to a  $2 \rightarrow 2$  scattering  $p_a + p_b \rightarrow k + q$  and a decay  $q \rightarrow k_1 + k_2$ , as depicted in Fig. 9. Exploiting Lorentz invariance of  $d\Phi_2$ , we compute the  $2 \rightarrow 2$  subprocess in the center-of-mass frame of the  $2 \rightarrow 3$  scattering, with the four-vectors defined as,

$$\begin{cases} p_a = (\frac{\sqrt{s}}{2}, 0, 0, \frac{\sqrt{s}}{2}) \\ p_b = (\frac{\sqrt{s}}{2}, 0, 0, -\frac{\sqrt{s}}{2}) \\ q = (E_q, 0, |\mathbf{q}| \sin \theta_1, |\mathbf{q}| \cos \theta_1) \\ k = (E_k, 0, -|\mathbf{q}| \sin \theta_1, -|\mathbf{q}| \cos \theta_1) \end{cases}, \quad (\text{B.3})$$

whereas the  $1 \rightarrow 2$  process is evaluated in the rest frame of the compound particle  $q$ , with the following parameterization of the four-vectors,

$$\begin{cases} q = (q, 0, 0, 0) \\ k'_1 = (E_{k'_1}, |\mathbf{k}'_1| \sin \theta_2 \cos \varphi_2, |\mathbf{k}'_1| \sin \theta_2 \sin \varphi_2, |\mathbf{k}'_1| \cos \theta_2) \\ k'_2 = (E_{k'_2}, -|\mathbf{k}'_1| \sin \theta_2 \cos \varphi_2, -|\mathbf{k}'_1| \sin \theta_2 \sin \varphi_2, -|\mathbf{k}'_1| \cos \theta_2) \end{cases}. \quad (\text{B.4})$$

In this expression, the energies and the 3-momenta are evaluated in the respective frames. The angles have been chosen in such a way that the decay frame is reached from the  $2 \rightarrow 2$  frame by a simple Lorentz transformation,  $R$ , consisting of a rotation followed by a boost along the  $\hat{x}$  axis,

$$R = \begin{pmatrix} E_q/q & 0 & 0 & -|\mathbf{q}|/q \\ 0 & 1 & 0 & 0 \\ 0 & 0 & 1 & 0 \\ -|\mathbf{q}|/q & 0 & 0 & E_q/q \end{pmatrix} \times \begin{pmatrix} 1 & 0 & 0 & 0 \\ 0 & 1 & 0 & 0 \\ 0 & 0 & \cos \theta_1 & -\sin \theta_1 \\ 0 & 0 & \sin \theta_1 & \cos \theta_1 \end{pmatrix}, \quad (\text{B.5})$$

where  $E_q, |\mathbf{q}|$  are defined in Eq. (B.3). The scalar products appearing in the amplitudes (4.4) and (4.5) are then evaluated in the  $2 \rightarrow 2$  frame by applying the  $R$  transformation:  $k_1 = R^{-1}k'_1$  and  $k_2 = R^{-1}k'_2$ . In our parametrization, the integration intervals are given by  $\theta_i \in [0, \pi]$ ,  $\varphi_i \in [0, 2\pi]$  and  $q^2 \in [4M^2, s]$ , where the muon and Higgs-boson masses have been neglected.

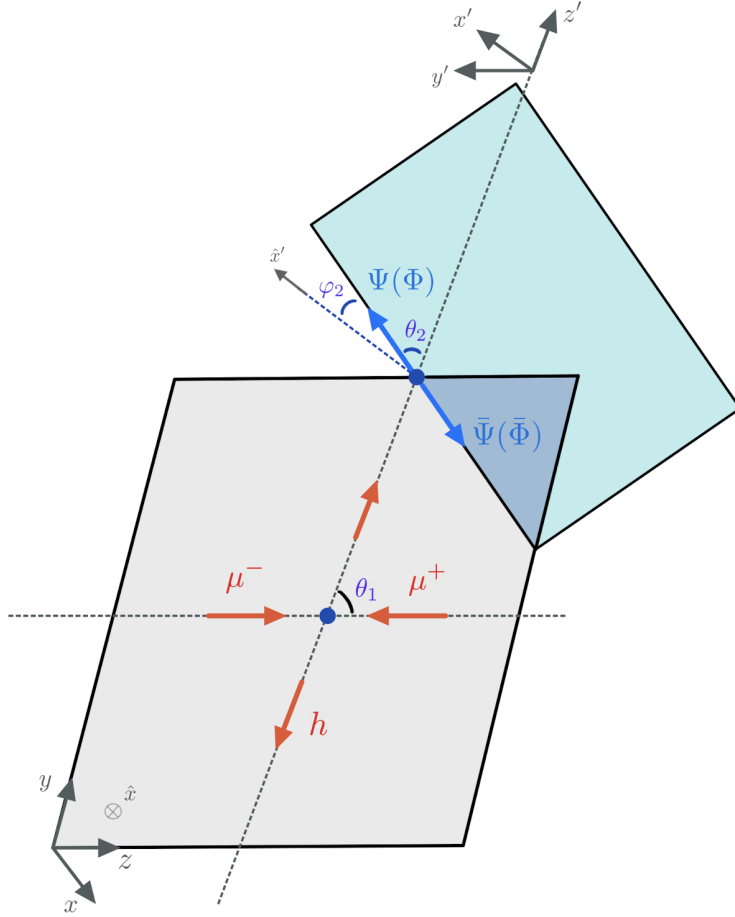


Figure 9: The two frames in which the two-body phase-spaces are evaluated. The grey plane is orthogonal to  $\hat{x}$  and it is defined in the center-of-mass frame, whereas the blue frame is defined with primed coordinates  $\hat{x}', \hat{y}', \hat{z}'$  in the rest-frame of the compound particle  $q$ .

## References

- [1] B. Abi *et al.* [Muon g-2 Collaboration], Phys. Rev. Lett. **126** (2021) no.14, 141801; T. Albahri *et al.* [Muon g-2 Collaboration], Phys. Rev. A **103** (2021) no.4, 042208; T. Albahri *et al.* [Muon g-2 Collaboration], Phys. Rev. D **103** (2021) no.7, 072002.
- [2] G. W. Bennett *et al.* [Muon g-2 Collaboration], Phys. Rev. D **73** (2006) 072003.
- [3] T. Aoyama *et al.*, Phys. Rept. **887** (2020) 1.
- [4] S. Borsanyi, Z. Fodor, J. N. Guenther, C. Hoelbling, S. D. Katz, L. Lellouch, T. Lippert, K. Miura, L. Parato and K. K. Szabo, *et al.* Nature **593** (2021) no.7857, 51-55.
- [5] M. Passera, W. J. Marciano and A. Sirlin, Phys. Rev. D **78** (2008) 013009; A. Keshavarzi, W. J. Marciano, M. Passera and A. Sirlin, Phys. Rev. D **102** (2020) no.3, 033002; A. Crivellin, M. Hoferichter, C. A. Manzari and M. Montull, Phys. Rev. Lett. **125** (2020) no.9, 091801;

- G. Colangelo, M. Hoferichter and P. Stoffer, JHEP **1902** (2019) 006; Phys. Lett. B **814** (2021) 136073.
- [6] C. M. Carloni Calame, M. Passera, L. Trentadue and G. Venanzoni, Phys. Lett. B **746**, 325-329 (2015); G. Abbiendi *et al.* Eur. Phys. J. C **77**, no.3, 139 (2017); A. Masiero, P. Paradisi and M. Passera, Phys. Rev. D **102**, no.7, 075013 (2020).
- [7] W. J. Marciano, A. Masiero, P. Paradisi and M. Passera, Phys. Rev. D **94**, no.11, 115033 (2016); M. Bauer, M. Neubert, S. Renner, M. Schnubel and A. Thamm, Phys. Rev. Lett. **124**, no.21, 211803 (2020); C. Cornella, P. Paradisi and O. Sumensari, JHEP **01**, 158 (2020).
- [8] W. Buchmuller and D. Wyler, Nucl. Phys. B **268** (1986) 621; B. Grzadkowski, M. Iskrzynski, M. Misiak and J. Rosiek, JHEP **1010** (2010) 085; E. E. Jenkins, A. V. Manohar and M. Trott, JHEP **1401** (2014) 035; R. Alonso, E. E. Jenkins, A. V. Manohar and M. Trott, JHEP **1404** (2014) 159.
- [9] See, e.g. G. F. Giudice, P. Paradisi and M. Passera, JHEP **11**, 113 (2012); A. Crivellin, M. Hoferichter and P. Schmidt-Wellenburg, Phys. Rev. D **98**, no.11, 113002 (2018); R. Dermisek, K. Hermanek, N. McGinnis and N. McGinnis, Phys. Rev. Lett. **126**, no.19, 191801 (2021); J. Aebischer, W. Dekens, E. E. Jenkins, A. V. Manohar, D. Sengupta and P. Stoffer, JHEP **07**, 107 (2021); S. Fajfer, J. F. Kamenik and M. Tamaro, JHEP **06**, 099 (2021); L. Allwicher, L. Di Luzio, M. Fedele, F. Mescia and M. Nardecchia, Phys. Rev. D **104**, no.5, 055035 (2021); P. Athron, C. Balázs, D. H. J. Jacob, W. Kotlarski, D. Stöckinger and H. Stöckinger-Kim, JHEP **09**, 080 (2021) and therein references.
- [10] R. Capdevilla, D. Curtin, Y. Kahn and G. Krnjaic, Phys. Rev. D **103**, no.7, 075028 (2021). R. Capdevilla, D. Curtin, Y. Kahn and G. Krnjaic, Phys. Rev. D **105**, no.1, 015028 (2022).
- [11] D. Buttazzo and P. Paradisi, Phys. Rev. D **104**, no.7, 075021 (2021).
- [12] J. P. Delahaye, M. Diemoz, K. Long, B. Mansoulié, N. Pastrone, L. Rivkin, D. Schulte, A. Skrinsky and A. Wulzer, [[arXiv:1901.06150](https://arxiv.org/abs/1901.06150) [physics.acc-ph]]; H. Al Ali, N. Arkani-Hamed, I. Banta, S. Benevedes, D. Buttazzo, T. Cai, J. Cheng, T. Cohen, N. Craig and M. Ekhterachian, *et al.* [[arXiv:2103.14043](https://arxiv.org/abs/2103.14043) [hep-ph]].
- [13] A. Crivellin and M. Hoferichter, JHEP **07** (2021), 135.
- [14] K. Kowalska and E. M. Sessolo, JHEP **09**, 112 (2017).
- [15] L. Calibbi, R. Ziegler and J. Zupan, JHEP **07**, 046 (2018).
- [16] K. m. Cheung, Phys. Rev. D **64** (2001), 033001.
- [17] I. Doršner, S. Fajfer and O. Sumensari, JHEP **06** (2020), 089.
- [18] A. E. Thomsen, Eur. Phys. J. C **81** (2021) no.5, 408.
- [19] H. H. Patel, Comput. Phys. Commun. **218** (2017), 66-70.
- [20] M. Chiesa, F. Maltoni, L. Mantani, B. Mele, F. Piccinini and X. Zhao, JHEP **09**, 098 (2020); T. Han, W. Kilian, N. Kreher, Y. Ma, J. Reuter, T. Striegl and K. Xie, JHEP **12** (2021), 162; D. Buttazzo, R. Franceschini and A. Wulzer, JHEP **05**, 219 (2021).